

Dark and stellar matter in strong lensing galaxies from a joint lensing and stellar dynamics^{*}

Takashi Hamana¹, Youichi Ohyama^{2,1}, Masashi Chiba³, Nobunari Kashikawa¹

¹ *National Astronomical Observatory of Japan, Mitaka, Tokyo 181-8588, Japan*

² *Institute of Space and Astronautical Science, Japan Aerospace Exploration Agency, Sagami-hara, Kanagawa 229-8510, Japan*

³ *Astronomical Institute, Tohoku University, Aoba-ku, Sendai 980-8578, Japan*

Accepted *****; Received *****; in original form 2005 July 4

ABSTRACT

We present Subaru spectroscopy of the early-type lensing galaxies in the lens systems HST 14113+5211 (at the redshift $z_L = 0.464$) and B 2045+265 ($z_L = 0.868$), being aimed at measuring the velocity dispersion of the lensing galaxies as an important component to their mass distributions and internal dynamics. For HST 14113+5211 we have obtained $174 \pm 20 \text{ km s}^{-1}$ (1σ) inside an aperture of $0.''9$, and for B 2045+265 we have obtained $213 \pm 23 \text{ km s}^{-1}$ inside an aperture of $1.''2$. To extract the significance of these information on the mass distributions and stellar dynamics of the lensing galaxies, we construct two alternative models for both the mass and velocity distributions. It is found that the mass-to-light ratios as derived from a joint lensing and stellar dynamics analysis are virtually consistent with those obtained from the use of the Fundamental Plane. Also, for HST 14113+5211, we find that the total mass distribution is well reproduced by a power-law density profile with an index of 2, thereby suggesting that a singular isothermal model is a good fit to the lensing galaxy. In contrast, the corresponding slope for B 2045+265 is flatter than isothermal, suggesting that additional contributions to lensing mass from surrounding structures (possibly the group of galaxies) provide the observed angular separations of multiple images.

Key words: cosmology: observations — gravitational lensing — quasars: individual (HST 14113+5211, B 2045+265)

1 INTRODUCTION

Massive early type galaxies are predicted to form at the highest density peaks in the early universe and to evolve through subsequent mass assemblies. Measuring their dynamical structure and stellar content over the cosmic time provides important constraints not only on their formation history itself but also on models of structure formation scenario and cosmic star formation history.

Studying the internal structure of early type galaxies is, however, difficult because of lack of dynamical tracers at large radii such like H_I gas in spirals, and of degeneracy between kinematic properties of dynamical tracers and mass distributions: The stellar dynamics suffers from the mass-anisotropy problem, and the gravitational lensing does from the mass-density profile problem as well.

Those degeneracies can be broken by combining those two probes, since they nicely complement each other (Treu &

Koopmans 2002; 2004 (hereafter TK04); Koopmans & Treu 2003). A combined analysis thus places important limits on the distributions of luminous and dark matter in a lensing early type galaxy.

We select two lens systems, HST14113+5211 ($z_L = 0.464$; Fischer, Schade & Barrientos 1998; Lubin et al. 2000) and B 2045+265 ($z_L = 0.868$; Fassnacht et al. 1999), where the lensing galaxies are an early-type galaxy. We conducted the direct measurement of velocity dispersion of the lensing galaxies of those systems using the Faint Object Camera and Spectrograph (FOCAS, Kashikawa et al. 2002) mounted on the Subaru Telescope. We perform a joint gravitational lensing and stellar dynamics analysis to explore the luminous and dark matter distribution of lensing galaxies focusing on the slope of (dark and total matter) density profile and mass-to-light ratio. Also, we utilize the fundamental plane relation of early type galaxies for deriving an alternative estimate of the mass-to-light ratio, which, after combined with the joint analysis, provides a useful constraint on the mass distribution of the lensing galaxy.

The paper is organized as follows. In §2, we show the

^{*} Based on data collected at Subaru Telescope, which is operated by the National Astronomical Observatory of Japan.

observations and data reduction. In §3, we derive the mass-to-light ratio of the lensing galaxies from the fundamental plane relation of early type galaxies. In §4, models for gravitational lensing and stellar dynamics are presented. §5 is devoted to the results of our model analysis, and discussion and concluding remarks are drawn in §6.

Throughout this paper, we adopt $\Omega_0 = 0.3$, $\lambda_0 = 0.7$, and $h = H_0/100 \text{ km s}^{-1} \text{ Mpc}^{-1} = 0.65$ for the relevant estimations.

2 VELOCITY DISPERSION MEASUREMENT

2.1 Observations

Spectroscopic observations were made with the Subaru 8.2m telescope (Iye et al. 2004). The FOCAS spectrograph (Kashikawa et al. 2002) was configured with a $0''.4$ -width slit, a 300 grooves mm^{-1} grism which gives 1.40\AA per pixel, and a Y47 order-cut filter to obtain optical spectra of the lensing galaxies of gravitational lens systems HST 14113+5211 and B 2045+265. The on-chip binning was set to 3 (along spatial direction to give $0''.3$ per pixel) by 1 (along wavelength direction).

For HST 14113+5211, observation was made on 2002 June 13 and 14 (UT). The slit was placed along the major axis of the lensing galaxy, whose position angles (PAs) was $\text{PA} = 38.1^\circ$. We obtained ten 1800 seconds exposures, and the total exposure time was 5 hours. For B 2045+265, observation was made on 2002 June 13 (UT). The slit was placed along the major axis of the lensing galaxy ($\text{PA} = 120.1^\circ$). We obtained seven 1800 seconds exposures, and the total exposure time was 3.5 hours. The seeing conditions were around $0.4'' - 0.8''$ during the two observing nights.

2.2 Data reduction

Basic data reductions were made following Ohyama et al. (2002). In the followings, we focus on the spectra of the lensing galaxies. Wavelength accuracy and resolution of the galaxy spectra were measured, within the wavelength region for the Fourier cross-correlation analyses (see section 2.4), by means of Gaussian fittings of several narrowest (unblended) sky OH lines. Here all measured values are shown in the rest frame of each galaxy, since all the following velocity dispersion measurements were made in their rest frames. For the spectrum of HST 14113+5211, we found that wavelength resolution is 4.5\AA FWHM at $4000 - 4450\text{\AA}$ (the blue fitting region) and 3.2\AA at $4780 - 5170\text{\AA}$ (the red fitting region). See below for details of the spectrum fitting regions). The wavelength accuracy is found to be typically $\simeq 0.09\text{\AA}$ in RMS over $3800 - 6500\text{\AA}$, and it gets slightly worse to $\simeq 0.28\text{\AA}$ at the bluest wavelength ($\sim 4000\text{\AA}$) for the cross-correlation analyses. For B 2045+265, wavelength resolution is 2.7\AA FWHM at $4100 - 4500\text{\AA}$, and wavelength accuracy is typically $\simeq 0.07\text{\AA}$ in RMS over $3800 - 4500\text{\AA}$. Aperture size to extract a 1-dimensional galaxy spectrum are $0''.9$ (3-binned pixel, corresponding to 8.3 kpc at $z = 0.464$ for the adopted cosmology) and $1''.2$ (4-binned pixel, 19 kpc at $z = 0.868$) for HST 14113+5211 and B 2045+265, respectively, to obtain spectra with maximum signal-to-noise quality.

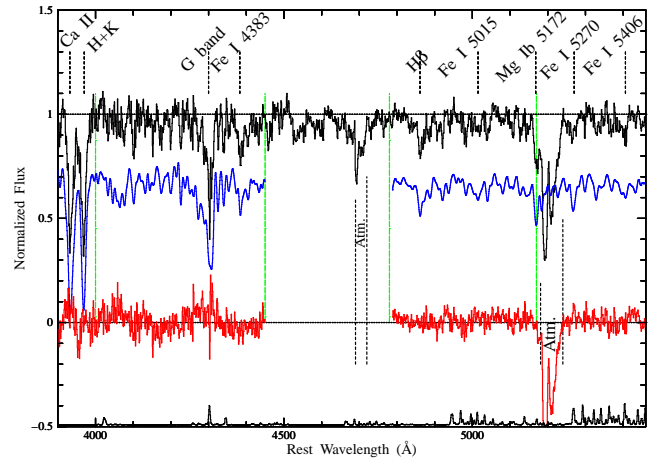


Figure 1. Continuum-normalized spectrum of HST 14113+5211 (*black*) in the rest frame of the galaxy. The continuum-normalized spectrum of a template star, HD 126778, after Gaussian-broadened to match the galaxy spectrum ($\sigma = 174 \text{ km s}^{-1}$), is shown (*blue*) with a vertical offset of -0.3 for clarity of the figure. Residual spectrum (galaxy – Gaussian-broadened template) (*red*) and a sky spectrum (*black*) are also shown. Here the sky spectrum is shown, with a vertical offset of -0.5 , to identify wavelength at which strong sky emission could damage the observed galaxy spectrum, and is flux-scaled by an arbitrary number. Atmospheric extinction features are marked with vertical black broken lines. Two wavelength regions used in the analyses of the velocity dispersion (blue and red fitting regions) are marked by two vertical *green* lines (see a main text for details of the wavelength fitting regions). Prominent features seen in the galaxy spectrum are identified as shown in upper portion of the figure.

2.3 Basic properties of the spectra

Reduced rest-frame spectra, after continuum normalization, are shown in Figures 1 and 2. For HST 14113+5211, deep Ca II H and K absorption lines and prominent G band feature are evidently seen in the spectrum, suggesting that major contribution in the observed wavelength region could be attributed to the late type giant stars (late G giant – early K giant stars). The redshift of the lensing galaxy is measured to be $z = 0.4644 \pm 0.0002$ from these prominent features, and is consistent with previous measurement (Lubin et al. 2000). In the redder part of the spectrum, several more features, including $\text{H}\beta$ and some Fe absorptions (Fe I 5270\AA and 5406\AA) are seen as well as Mg Ib 5172\AA which is partly detected at the blue edge of the atmospheric absorption feature (the A band).

For B 2045+265, although signal-to-noise ratio of the observed spectrum is worse than that of HST 14113+5211 due to both fainter apparent brightness and shorter exposure time achieved for the galaxy, we have clearly detected Ca II H and K absorption lines and G band feature (Fig 2). We note, however, that these features are less prominent than those of HST 14113+5211. We also note that B 2045+265 shows another possible prominent absorption feature at just red edge of the A band feature. We checked this possibility by comparing the A band features of both galaxies in the observed frame (at 7660\AA), and confirmed that B 2045+265 shows an excess absorption over expected A-band feature. This feature, at 4100\AA in the rest frame, can be identified as $\text{H}\delta$ absorption, although another Balmer

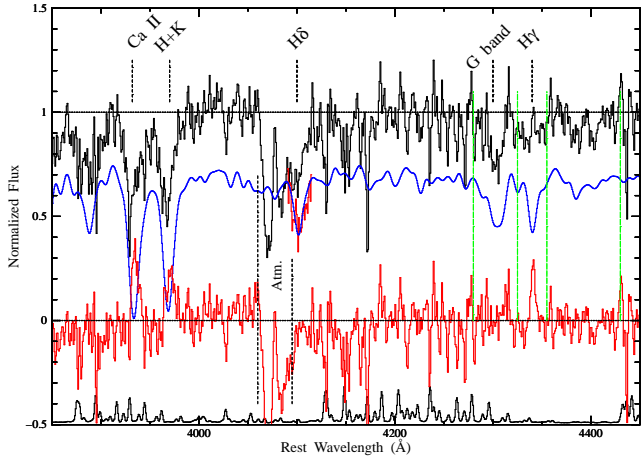


Figure 2. Same as figure 1, but for B 2045+265. The sky spectrum is flux-scaled by a same amount as used for figure 1. Expected contribution of the galaxy absorption over the atmospheric A band absorption near 4100Å is shown in red, with a vertical offset of -0.3 , overlaying the Gaussian-broadened ($\sigma = 213 \text{ km s}^{-1}$) template spectrum of HD 136202. See a main text for details of this feature.

absorption line, $H\gamma$ near the G band, was not detected. Since $H\gamma$ emission is ~ 1.8 times brighter than $H\delta$ emission under the “case B” photoionization, which is typical for star-forming regions, difference in the observed properties of Balmer lines can be naturally understood. Note that more higher-order Balmer absorptions were identified by Fassnacht et al. (1999). Prominent [OII] emission is also detected, suggesting a star-forming activity in this galaxy. Fassnacht et al. (1999) classified the spectrum as the Sa type, and are best represented by giant stars of late F type. The redshift of the lensing galaxy is measured to be $z = 0.8682 \pm 0.0001$ by [OII] emission, which is consistent with that measured by prominent absorption lines, although it is slightly larger than the value measured by Fassnacht et al. (1999) ($z = 0.8673 \pm 0.0005$).

2.4 Fourier cross-correlation analysis

We basically followed the procedure of Ohyama et al. (2002), and the Fourier cross-correlation method (Tonry & Davis 1979) was used to measure the line-of-sight velocity dispersion of the lensing galaxies with the FXCOR task implemented in IRAF¹ (see also Falco et al. 1997). Here we outline our procedure applied for both galaxies. Firstly, velocity-resolution matched stellar spectra were created from the “C ode feed spectral library” spectra (Leitherer et al. 1996), whose wavelength resolutions are 1.8Å FWHM for both red and blue spectra in the library, to match the resolution of the observed galaxy spectra, and were used as “templates” which are to be fitted with the observed galaxy spectra. Secondly, calibration curves, which relate the velocity dispersion of Gaussian broadening function applied to the templates

¹ IRAF is distributed by the National Optical Astronomy Observatories, which are operated by the Association of Universities for Research in Astronomy, Inc., under cooperative agreement with the National Science Foundation.

Table 1. Properties of template stars: (1) star name, (2) spectral type, (3) effective temperature (K), (4) surface gravity in log and (5) metal abundance in units of solar metallicity.

Star ⁽¹⁾	Type ⁽²⁾	T_{eff} ⁽³⁾	$\log g$ ⁽⁴⁾	[Fe/H] ⁽⁵⁾
for HST 14113+5211				
HD 206453	G8III	5092	2.14	-0.42
HD 1918	G9III	4865	2.01	-0.47
HD 126778	K0III	4847	2.34	-0.53
for B 2045+265				
BD+11 2998	F8III	5425	2.30	-1.17
HD 136202	F8III-IV	6030	3.89	-0.07

to the width of the cross-correlation functions (CCF) peak, were created. Finally, curves were used to find the velocity dispersion of the galaxy from the CCF peak width calculated between the observed galaxy spectra and the templates. FXCOR parameters were kept unchanged from that used by Ohyama et al. (2002) except for template stars and fitting wavelength regions to match the spectral properties of the program galaxies in this work.

2.4.1 HST 14113+5211

For HST 14113+5211, we choose two separate wavelength regions ($4000 - 4450\text{Å}$ and $4780 - 5170\text{Å}$, hereafter blue and red fitting regions, respectively) to be used in the FXCOR, which include most of the prominent absorption features, such as G band, Fe I, and $H\beta$, while avoiding atmospheric absorption features (A and B bands). Fe I features at $5250 - 5410\text{Å}$ are not included in the analyses because they are detected at redder part of the A band and available wavelength region around them is not wide enough. The Ca II H and K features were also excluded from the fitting regions, since the calculation with these features might give problematic result because of their intrinsically wider line width (Tonry 1998). We choose late type giant stars with sub-solar metallicity as spectral templates, since we found during the course of the spectrum fitting that stars with nearly solar metallicity show deeper Fe I absorptions than the observed ones. We choose three such stars, HD 206453, HD 1918, and HD 126778 (see Table 1 for their detailed properties)². For each star, blue ($3820 - 4500\text{Å}$) and red ($4780 - 5450\text{Å}$) spectra are available in the spectral library, and each of them was used separately in the FXCOR for fitting blue ($4000 - 4450\text{Å}$) and red ($4780 - 5170\text{Å}$) fitting regions, respectively. Red and blue template spectra were processed separately in both the continuum normalization and velocity resolution matching procedures, and then each template was used separately in the FXCOR to make two calibration curves for a set of one template star and the galaxy.

We made FXCOR runs twelve times for each template (three stars), fitting region (two regions per star), and CCF

² Metallicity of the selected template stars ([Fe/H] = $-0.4 - -0.5$) is by no means the best estimated value for the galaxy. They are arbitrarily chosen from a small subsample of low-metal stars in the spectral library.

Table 2. Results of Fourier cross-correlation analyses for HST 14113+5211. (1) The blue and red fitting regions are 4000 – 4450Å, and 4780 – 5170Å respectively. (2) R denotes Tonry-Davis R value.

Star	CCF fitting width	blue ⁽¹⁾		red ⁽¹⁾	
		σ (km s ⁻¹)	$R^{(2)}$	σ (km s ⁻¹)	$R^{(2)}$
HD 206453	30	173	16.6	162	13.7
	35	172	16.6	159	13.6
HD 1918	30	175	15.5	179	14.0
	35	172	16.6	170	14.1
HD 126778	30	191	17.8	170	14.7
	35	190	18.0	168	14.8
<i>R</i> -weighted average σ : for each fitting region		179±9 km s ⁻¹		168±7 km s ⁻¹	
for both fitting regions		174±10 km s ⁻¹			

peak width measurement lag (two lags, 30 and 35, per set of template and fitting region; see Ohya et al. 2002 for details of the parameter) to measure velocity dispersion of HST 14113+5211. We found that all cross-correlations between the galaxy and templates gave good Tonry-Davis R values ($R = 14 - 18$; Tonry and Davis 1979), suggesting that templates adopted for HST 14113+5211 could represent the galaxy spectrum well. We found that error of the galaxy velocity dispersion, originating from the error in measuring the CCF peak widths, was typically $\simeq 10$ km s⁻¹ (1σ). Averaging all the FXCOR results with a weight of R s, we obtained $\sigma = 179 \pm 9$ km s⁻¹ and 168 ± 7 km s⁻¹ in blue and red fitting regions, respectively. Here, errors represent 1σ scatters of the velocity dispersion values among all FXCOR runs. Another source of error, the velocity resolution matching error, estimated from the error in measuring the spectral resolution of the galaxy spectrum, could amount to $\simeq 14$ km s⁻¹ and $\simeq 7$ km s⁻¹ of galaxy velocity dispersion error (1σ) for blue and red fitting regions, respectively. Considering all sources of uncertainties (errors in velocity-resolution matching, CCF peak width measurement, and scattering of the velocity dispersion values among FXCOR runs), the overall 1σ uncertainties are estimated to be 19 ($\sqrt{14^2 + 10^2 + 9^2}$) and 13 ($\sqrt{7^2 + 10^2 + 7^2}$) km s⁻¹ for blue and red fitting regions, respectively. Note that results measured in two fitting regions are consistent to each other within expected errors. Therefore, averaging all twelve FXCOR results made in blue and red fitting regions, we adopt $\sigma = 174 \pm 20$ km s⁻¹ as the best estimated line-of-sight velocity dispersion of HST 14113+5211. Here, an error is estimated, based on velocity matching error of 14 km s⁻¹ (larger value out of two fitting regions), CCF fitting error of 10 km s⁻¹, and scattering among all FXCOR results (10 km s⁻¹; see Table 2), to be 20 ($\sqrt{14^2 + 10^2 + 10^2}$) km s⁻¹.

Fig 1 compares the spectrum of HST 14113+5211 with the best template, HD 126778, giving the best R values for both blue and red fitting regions, after Gaussian-broadened with velocity dispersion of $\sigma = 174$ km s⁻¹. We also show residual spectrum (galaxy – Gaussian-broadened template) along with the sky spectrum. All the spectra are shown over wider wavelength region, covering other spectral features not used for the FXCOR analyses, to show the overall quality of the spectral fitting. One may find that the broadened template gives rather good representation of the observed galaxy spectrum over entire wavelength region, except for

a large-scale residual pattern in the blue continuum. The residual feature likely comes from errors in fitting the continuum spectra of both the galaxy and the templates, used for continuum normalization. Since the continuum fittings were made over the wavelength regions where spectra show rather large-amplitude change in shape, an artificial large-scale spectral variation could be easily introduced into the continuum-normalized spectra. Note, however, that this error does not affect our cross-correlation results, since such a low-frequency variation in spectral shape is filtered out in the FXCOR before calculating the CCF (see Ohya et al. 2002 for more details on the FXCOR parameters). In concluding, after considering the fitting quality as discussed above, we finally adopt $\sigma = 174 \pm 20$ km s⁻¹ as the best estimated velocity dispersion of HST 14113+5211 in the following lens analysis.

2.4.2 B 2045+265

For B 2045+265, we followed the same procedure used for HST 14113+5211. However, because of relatively poor quality of B 2045+265 spectrum, only a narrow wavelength region, comprising two smaller wavelength regions of 4280 – 4325Å and 4355 – 4430Å, was chosen for the FXCOR analyses. The spectral regions were carefully chosen to include G band while avoiding both the strong sky emission regions and H γ , and these two smaller regions were fitted at a same time in FXCOR. Here, the H γ was excluded in the fitting since H γ emission may overlay underlying H γ absorption. We choose two late F giant stars, BD+11 2998 and HD 136202, as spectral templates for the galaxy from the same spectral library (see Table 1 for their detailed properties)³. We ran FXCOR four times (for one fitting region, two template stars, and with two CCF peak width measurement lags), and found that R values are rather large, 30 – 40, for all FXCOR runs. The larger R values probably result from the fact that we have only one prominent spectral feature (G band) in a narrow wavelength region for fitting. The best estimated velocity dispersion is $\sigma = 213$ km s⁻¹, with an 1σ error of ± 11 km s⁻¹ originating from scattering of

³ Again, as in the case of the analyses of HST 14113+5211, metallicity of the selected template stars is by no means the best estimated value for the galaxy.

Table 3. Same as Table 2 but for B 2045+265. Fitting region is 4280 – 4325Å plus 4355 – 4430Å.

Star	CCF fitting width	σ (km s ⁻¹)	R
BD+11 2998	30	219	30.9
	35	234	30.5
HD 136202	30	210	39.9
	35	213	39.7
R -weighted average σ :		213±11 km s ⁻¹	

the σ values among all FXCOR runs (see Table 3). The velocity resolution-matching error could amount to $\simeq 5$ km s⁻¹ of galaxy velocity dispersion error (1σ), which is smaller than in the case of HST 14113+5211 due to higher redshift of B 2045+265. We found that error of the galaxy velocity dispersion, originating from the error in measuring the CCF peak widths, was typically $\simeq 19$ km s⁻¹ (1σ), which is larger than the value for HST 14113+5211 because of relatively poor CCF determination resulting from lower quality spectrum and narrower wavelength fitting regions available for B 2045+265. Considering all sources of uncertainties (errors in velocity-resolution matching, CCF peak width measurement, and scattering of the velocity dispersion values among FXCOR runs), the overall 1σ uncertainty is estimated to be $23 (\sqrt{5^2 + 19^2 + 11^2})$ km s⁻¹.

Fig 2 compares the observed galaxy spectrum with the Gaussian-broadened template spectrum of the best template, HD 136202, after Gaussian-broadened with the velocity dispersion of $\sigma = 213$ km s⁻¹, as in the same way for HST 14113+5211. One may find that the broadened template gives rather good representation of the galaxy spectrum over entire wavelength region, including H δ , except for H γ and Ca II H and K features. We expect that the residual emission of H γ represents the real emission, overlaying on the absorption line, as expected from another emission line of [OII]. On the other hand, it seems difficult to attribute the shallower-than-observed Ca II absorptions in the broadened template spectrum to overlaying emissions. Although putative H ϵ emission, whose wavelength is almost coincident with that of Ca II H absorption, might explain a part of the residual feature, there seems no emission lines which could be coincident with Ca II K feature neither in the spectra of the lens galaxy nor the lensed QSO. Therefore, the most simple and plausible explanation for the shallower observed Ca II absorption is that the lensing galaxy contains not only stars of late F type but also of even earlier types. Although neglecting the contribution of the earlier population in the FXCOR analyses should affect the velocity dispersion measurement, we expect that our result, made assuming a pure stellar population of late F type as spectral templates, is still reasonably reliable and is useful for our analyses on the mass model and the stellar dynamics in the following sections. This is because (1) stars of earlier types show much shallow G band feature, and they can not fit the observed spectrum alone, indicating that late F stars contribute most to the observed spectrum in flux, and (2) our measurement almost relies on the spectral fit of the G band feature and, hence, the velocity dispersion measured in our analyses lies larger weight on the later type stars, which contribute much more on the mass of the lensing galaxy than the case of stars of earlier types. Therefore, we adopt $\sigma = 213 \pm 23$ km

s⁻¹ as the best estimated line-of-sight velocity dispersion of B 2045+265 in the following lens analysis.

3 FUNDAMENTAL PLANE

Before going into a joint gravitational lensing and stellar dynamics, let us examine the Fundamental Plane (FP) for early type galaxies, which provides us with an alternative insight into the value of the mass-to-light ratio M_*/L_B . The FP is defined by the effective radius (R_e kpc), central velocity dispersion (σ_c km s⁻¹), and mean surface brightness inside R_e (SB_e mag arcsec⁻²):

$$\log R_e = \alpha_{FP} \log \sigma_c + \beta_{FP} SB_e + \gamma_{FP}, \quad (1)$$

where $\alpha_{FP} = 1.25$, $\beta_{FP} = 0.32$, and $\gamma_{FP} = -8.895 - \log h_{50}$ ($h_{50} = H_0/50$ km s⁻¹ Mpc⁻¹) in the B band (Bender et al. 1998). The central velocity dispersion σ_c is taken as the velocity dispersion measured inside $R_e/8$ (TK04).

For the lensing galaxy of HST 14113+5211, Fischer, Schade, & Barrientos (1998, hereafter F98) obtained the rest-frame central surface brightness of the lensing galaxy as $\mu_{0,B}(AB) = 13.57$ mag arcsec⁻². Then, as the surface brightness at $R_e = 0.''61 \pm 0.''03$ (F98) is $\mu_{e,B}(AB) = \mu_{0,B}(AB) + 8.33$ and $B(\text{Vega}) = B(AB) + 0.12$, we obtain the surface brightness at R_e as $\mu_{e,B} = 22.02$ mag arcsec⁻². The mean surface brightness within R_e is then estimated as $SB_e = 20.56$ mag arcsec⁻² after correction for Galactic extinction $E(B - V) = 0.016$ mag (Schlegel, Finkbeiner, & Davis 1998) and an $R_V = 3.1$ extinction curve. Alternatively, van de Ven, van Dokkum, & Franx (2003, hereafter vdV03) derived $\mu_{e,B} = 21.70$ mag arcsec⁻² at the intermediate effective radius R_e of $0.''48$ (Kochanek et al. 2000), giving $SB_e = \mu_{e,B} - 1.393 \simeq 20.56$ mag arcsec⁻². As the small difference between these values results in only the difference of 0.2 to 0.3 in the mass-to-light ratio obtained below, we adopt the results of F98 in what follows.

For the lensing galaxy of B 2045+265, we adopt the values given in vdV03, i.e., $R_e = 0.''38^{+0.''15}_{-0.''11}$ and $SB_e = \mu_{e,B} - 1.393 \simeq 19.11 \pm 0.44$ mag arcsec⁻².

To derive a fiducial correction factor from the measured σ in a specific aperture to σ_c in equation (1), we utilize a fiducial model for internal mass distribution and stellar dynamics as explained in §4. Briefly saying, we adopt a single mass component represented by a power-law density profile with an index of γ' [see equation (5)] and the velocity dispersion of stars represented by a constant anisotropy parameter β [see equation (6)]. For HST 14113+5211, we obtain $\sigma_c = 1.15\sigma$ based on the most likely parameters of $(\gamma', \beta) = (1.93, 0.14)$ (see §5) thereby yielding $\sigma_c = 200.7$

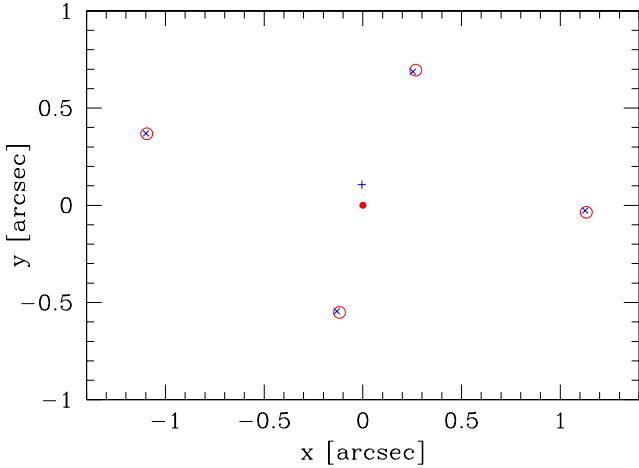


Figure 3. Lens configuration of the HST 14113+5211 compared with SIE lens with an external shear model. Multiple image positions and source position of the best-fitting model are shown by crosses and plus, respectively. Open circles show the observed image positions, where the radii of the circles correspond to $1\text{-}\sigma$ observational uncertainties. The lensing galaxy position is shown by filled circle and is taken as the coordinate origin.

km s^{-1} . For B 2045+265, we obtain $\sigma_c = 0.99\sigma$ based on the most likely parameters of $(\gamma', \beta) = (1.66, 0.10)$, thereby yielding $\sigma_c = 210.3 \text{ km s}^{-1}$.

Inserting into equation (1), we obtain $\gamma_{FP} = -8.87$ for the lensing galaxy of HST 14113+5211 at $z_L = 0.464$ and $\gamma_{FP} = -8.52$ for the lensing galaxy of B 2045+265 at $z_L = 0.87$. Comparison with γ_{FP} at $z = 0$ allows us to derive the difference in γ_{FP} , $\Delta\gamma_{FP}$, and then $\Delta\log(M_*/L_B) \equiv -0.4\Delta\gamma_{FP}/\beta_{FP}$ provided α_{FP} and β_{FP} are constant. We then obtain $\Delta\log(M_*/L_B) = -0.172$ for the lensing galaxy of HST 14113+5211 and -0.612 for the lensing galaxy of B 2045+265. The mass-to-light ratio at $z > 0$ is given as,

$$\log(M_*/L_B)_z = \log(M_*/L_B)_0 + \Delta\log(M/L_B) \quad (2)$$

where $(M_*/L_B)_0 = 7.3 \pm 2.1 h_{65} M_\odot/L_{B,\odot}$ (Gerhard et al. 2001). We obtain $(M_*/L_B)_z = 4.9 \pm 1.4 M_\odot/L_{B,\odot}$ for the lensing galaxy of HST 14113+5211 and $1.8 \pm 0.5 M_\odot/L_{B,\odot}$ for the lensing galaxy of B 2045+265. As will be shown below, these values of M_*/L_B for both systems are in good agreement with those obtained from a joint lensing and dynamical analysis (see §5).

4 MASS MODEL AND STELLAR DYNAMICS

4.1 Lens models

Following TK04, we model the lensing galaxy as a singular isothermal ellipsoid (SIE; Kormann, Schneider & Bartelmann 1994). Note that the Einstein radius (R_E) and mass enclosed by the Einstein radius (M_E), both of which are the quantities required in the dynamical model of the lensing galaxy in the following sections, are very insensitive to the assumed mass model (Kochanek 1991; Koopmans & Treu 2004). We also allow for a constant external shear. The observed position of a lensing galaxy is taken by a lens position and we do not treat the lens position as a

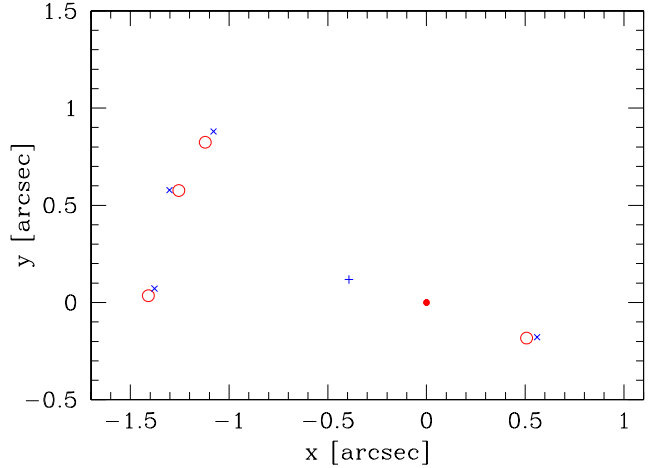


Figure 4. Same as Fig. 3 but for B 2045+265.

Table 4. Best-fitting model parameters and characteristic values of the singular isothermal ellipsoid with an external shear lens

Parameter	HST 14113+5211	B 2045+265
b_l (arcsec)	0.84	1.11
q_l	0.68	0.68
θ_l (deg)	38	-69
γ_{ext}	0.26	0.05
θ_{ext} (deg)	-35	18
β_x (arcsec)	-0.005	-0.39
β_y (arcsec)	0.11	0.12
σ_{SIE} (km/s)	202	397
R_E (kpc)	5.29	9.19
$M(< R_E)(M_\odot)$	1.58×10^{11}	1.06×10^{12}

free parameter. Therefore, our lens model has five parameters (we follow the notations in TK04); the lensing strength ($b_l = 4\pi(\sigma_{\text{SIE}}/c)^2 D_{ls}/D_s$, where σ_{SIE} is the one-dimensional velocity dispersion of SIE lens), axis ratio (q_l), position angle of the lens (θ_l), strength of the external shear (γ_{ext}), and its orientation (θ_{ext}). Also we treat the source position (β_x, β_y) as a free parameter.

We search for a set of model parameters that best reproduces the observed lens configuration. The best-fitting model parameters are summarized in Table 4. Figs 3 and 4 compare the observed image positions with the model images. The usual χ^2 values are 0.71 and 14 for HST14113+5211 and B 2045+265, respectively (for $1\text{-}\sigma$ observational uncertainties of 0.03 arcsec) and the number of degrees of freedom is $N_{\text{dof}} = 1$ (8 constraints and 7 parameters). As is evidently shown in Fig 3, for HST14113+5211, the model reproduces the lens configuration very well. The Einstein radius and mass enclosed by the Einstein radius are found to be $R_E = 5.29 \text{ kpc}$ and $M(< R_E) = 1.58 \times 10^{11} M_\odot$ (for the adopted cosmological parameters), respectively. On the other hand, for B 2045+265, although the model nicely reproduces the cusp-lensing configuration (Schneider Ehlers & Falco 1992), the best-fitting model positions slightly deviate from the observed positions. Since the enclosed mass is not very sensitive to a detail lens model but is primarily determined by the image separation, the best-fitting model may give a good estimate of the the enclosed mass. The Ein-

stein radius and mass enclosed are found to be $R_E=9.19\text{kpc}$ and $M(< R_E) = 1.06 \times 10^{12} M_\odot$, respectively, which we adopt in the following joint lensing and stellar dynamics analysis.

4.2 Mass model and stellar dynamics

Let the luminous-mass density and dark-matter density profiles be $\rho_{lum}(r)$ and $\rho_{DM}(r)$, respectively, provided that these are spherically symmetric. Two alternative mass models will be employed, following TK04.

First, we consider a two-component mass model, where the luminous mass and dark matter distribute differently:

$$\rho_{lum}(r) = \frac{M_* r_*}{2\pi r (r + r_*)^3} \quad (3)$$

$$\rho_{DM}(r) = \frac{\rho_{DM,0} r_b^3}{r^\gamma (r^2 + r_b^2)^{(3-\gamma)/2}}, \quad (4)$$

where M_* is the total stellar mass and r_* denotes the scale length for the luminous matter. The profile $\rho_{lum}(r)$ corresponds to a Hernquist model (Hernquist 1990), reproducing the $R^{1/4}$ surface brightness profile with an effective radius of $R_e = 1.8153r_*$. For M_* , we use the B -band total luminosity of the lensing galaxy, L_B , based on the mass-to-light ratio of the luminous matter, M_*/L_B , as a model parameter. Our estimation of L_B is given in Appendix, yielding $L_B/L_{B,\odot} = 2.6 \times 10^{10}$ and 1.3×10^{11} ($h = 0.65$) for the lensing galaxies of HST 14113+521 and B 2045+265, respectively. The dark-matter density profile, $\rho_{DM}(r)$, is determined by the scale length (r_b), density scale ($\rho_{DM,0}$), and inner slope (γ). The combination of all of these parameters will be constrained by the results of the lens fitting, R_E and $M(< R_E)$, as obtained in §4.1.

Second, we consider a single component with power-law mass model:

$$\rho_{tot}(r) \propto r^{-\gamma'}, \quad (5)$$

where γ' denotes an effective slope.

The velocity distribution of the stars is also assumed to be spherically symmetric, such that the velocity dispersions in spherical coordinates ($\sigma_r, \sigma_\theta, \sigma_\phi$) satisfy $\sigma_\theta = \sigma_\phi$ (e.g., Binney & Tremaine 1987). We then use the parameter $\beta(r) = 1 - \sigma_\theta^2/\sigma_r^2$ describing the degree of velocity anisotropy. We employ the following two models for $\beta(r)$, the Osipkov-Merritt model with a parameter r_i (referred to as Model A) and constant anisotropy model with a parameter β (Model B).

$$\beta(r) = \begin{cases} \frac{r^2}{r^2 + r_i^2}, & \text{for Model A} \\ \text{const.} (= \beta), & \text{for Model B} \end{cases} \quad (6)$$

Relevant parameters are r_i and β .

5 RESULTS OF A JOINT LENSING AND DYNAMICAL ANALYSIS

Based on the models given in the previous section, we search for the best mass model for reproducing the observed velocity dispersion σ using the joint lensing and dynamical analysis and also combining with the FP constraints. We especially focus on the best values of M_*/L_B

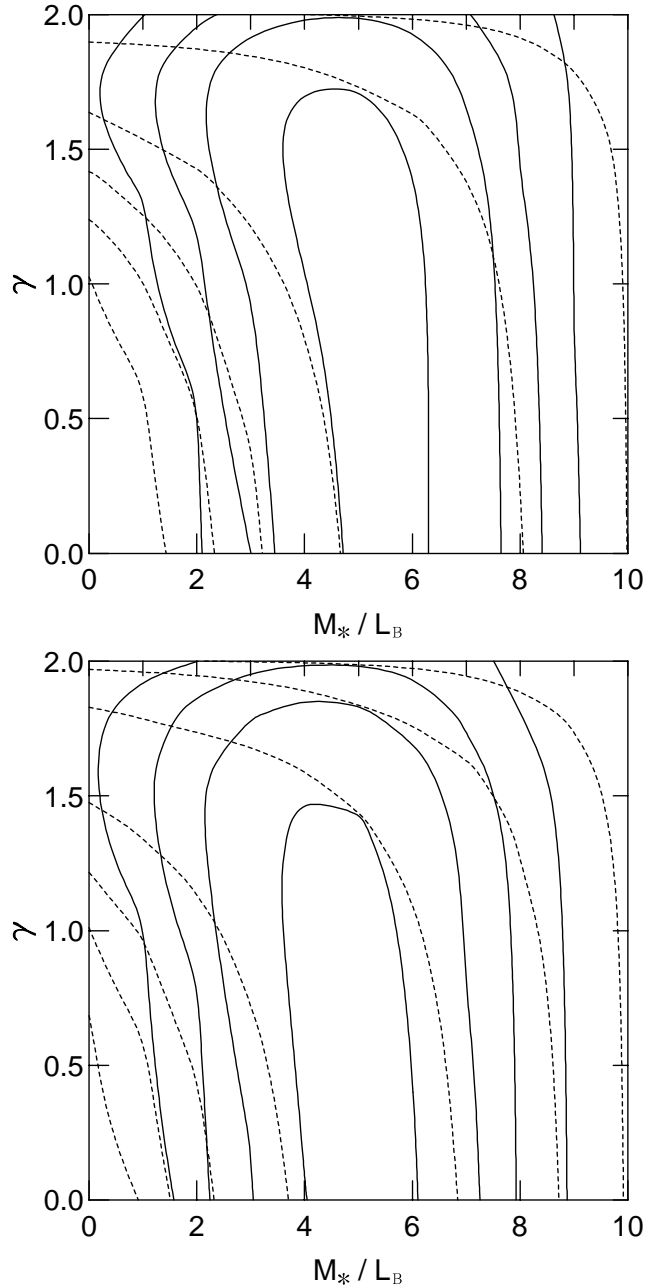


Figure 5. Likelihood contours for a joint lensing and dynamical analysis of HST 14113+5211 based on the two-component mass model. Contours show 68 % (1σ), 95 %, 99 %, and 99.9 % confidence levels. Dashed lines are derived from the current joint analysis, while solid lines combine the additional constraints from the FP plane. Lower panel: Model A with $r_i = R_e$ and $r_b = R_E$. Upper panel: Model B with $\beta = 0$ and $r_b = R_E$.

for a two-component model, which are to be compared with those from the FP constraints. Also, the inner slope of the dark-matter halos, γ , are to be compared with the prediction of cosmological N-body simulations [e.g., $\gamma = 1 - 1.5$ (Navarro, Frenk, & White 1995; Moore et al. 1998; Fukushige & Makino 2003 and references therein)]. For a single-component model, the derived slope γ' can be used to assess the isothermality of the lens density profile as usually adopted in other lensing work.

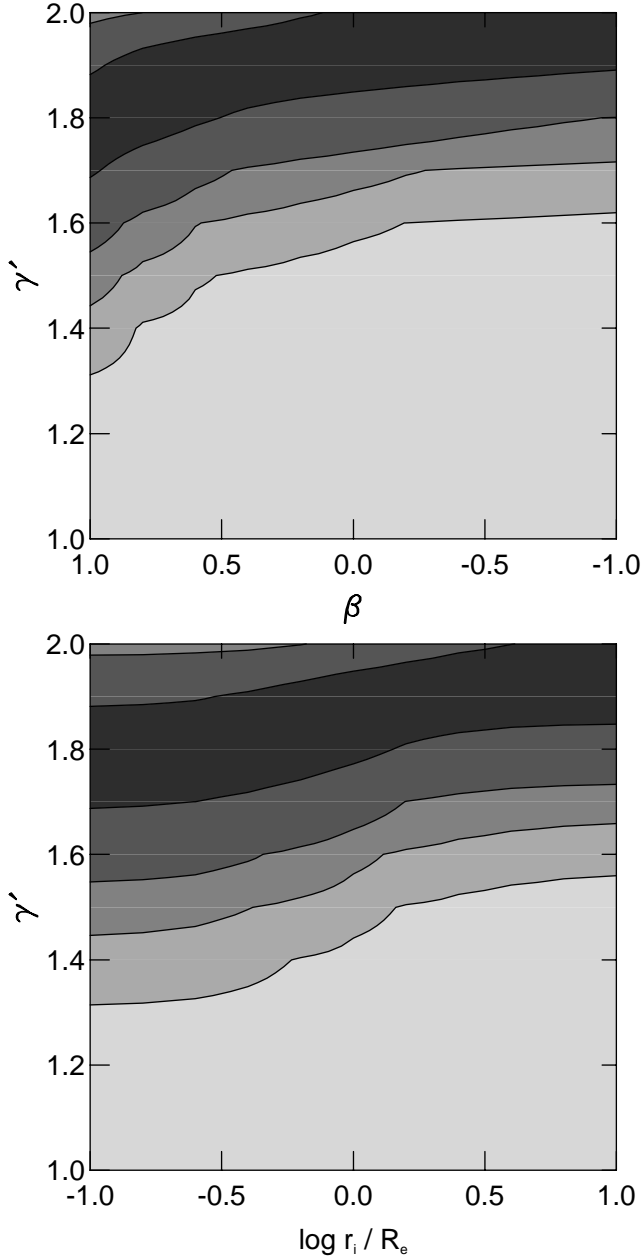


Figure 6. Likelihood contours for a joint lensing and dynamical analysis of HST 14113+5211 based on the single component with power-law mass model. Contours show 68 % (1σ), 95 %, 99 %, and 99.9 % confidence levels. Lower and upper panels are for Model A and Model B, respectively.

5.1 HST 14113+5211

First, we examine a two-component mass model. Figure 5 shows 68 % (1σ), 95 %, 99 %, and 99.9 % confidence levels of the likelihood contours in the plane of γ' and M_*/L_B when we adopt the velocity dispersion of $\sigma = 174 \pm 20 \text{ km s}^{-1}$. Dashed lines are derived from the joint lensing and dynamical analysis, while solid lines combine the additional constraints from the FP plane. For the lower panel (Model A) we set $r_i = R_e$ and $r_b = R_E$, and for the upper panel (Model B) we set $\beta = 0$ and $r_b = R_E$. The likely γ' or M_*/L_B using these parameter sets will be utilized as a characteristic

case in what follows, as the likelihood contours are found to remain basically the same in other parameter settings (TK04).

From the results based on the current joint analysis (dashed lines), the likely mass-to-light ratio appears to be in the range of $4 \lesssim M_*/L_B \lesssim 6 M_\odot/L_{B,\odot}$: after marginalizing over γ' , we obtain the most likely values of M_*/L_B ($M_\odot/L_{B,\odot}$), yielding $4.4^{+2.0}_{-2.1}$ for Model A and $5.6^{+2.2}_{-2.2}$ for Model B. As is evident, these values of M_*/L_B are virtually consistent with those obtained from the FP in §3 ($4.9 \pm 1.4 M_\odot/L_{B,\odot}$). We also calculate the most likely fraction of the dark matter projected inside R_E ($\simeq 1.4R_e$), which is denoted as f_{DM} . Adopting the isotropic velocity model as a representative case, we obtain $f_{DM} = 0.47^{+0.21}_{-0.21}$, suggesting that about a half of the total mass derived from the lens model constitutes dark matter.

Turn next to the result from the joint analysis combined with the FP constraints (plotted by the solid lines). Since the above joint analysis gives M_*/L_B being in a good agreement with one from the FP, the additional constraint from the FP makes only a minor change in the preferred M_*/L_B value. It is found that marginalized constraints on M_*/L_B ($M_\odot/L_{B,\odot}$) are $4.8^{+1.1}_{-1.2}$ for Model A and $5.1^{+1.2}_{-1.1}$ for Model B. The most likely fraction of the dark matter projected inside R_E (for the isotropic velocity case) reads $f_{DM} = 0.52^{+0.10}_{-0.12}$. The additional constraint from the FP improves the limit on γ' . We obtained, after marginalizing over M_*/L_B , a constraint on γ' to be $\gamma' < 1.6$ ($\gamma' < 1.8$) at $1\text{-}\sigma$ for Model A (Model B).

Second, we examine a single-component mass model to set limits on the slope γ' . Figure 6 shows 68 % (1σ), 95 %, 99 %, and 99.9 % confidence levels of the likelihood contours. We set $r_b = 3R_E$ in this diagram, but the limits on γ' are found to be little affected as long as $r_b \gtrsim 3R_E$. We estimate the most likely values of γ' for $r_i = R_e$ (Model A) and $\beta = 0$ (Model B), yielding $1.87^{+0.08}_{-0.09}$ and $1.94^{+0.07}_{-0.09}$, respectively. Thus, the total density profile is well approximated as $\rho_{tot}(r) \propto r^{-2}$.

5.2 B 2045+265

For the lensing galaxy of B 2045+265, we show the results in Figure 7 and 8, which are to be compared with Figure 5 and 6, respectively, obtained for HST 14113+5211.

For a two-component mass model (Figure 7), the likely mass-to-light ratio appears to be in the range of $0.7 \lesssim M_*/L_B \lesssim 2 M_\odot/L_{B,\odot}$: after marginalizing over γ' , we obtain the most likely values of M_*/L_B ($M_\odot/L_{B,\odot}$) for Model A (Model B) as $M_*/L_B = 0.8^{+0.5}_{-0.7}$ ($1.2^{+0.5}_{-0.7}$) without the FP constraints. As is evident, these values of M_*/L_B are also consistent with those obtained from the FP in §3 ($1.8 \pm 0.5 M_\odot/L_{B,\odot}$). Combining the FP constraint and after marginalizing over M_*/L_B we obtain $\gamma' < 0.5$ ($\gamma' < 0.8$) at 1σ for Model A (Model B). Thus the models prefer flatter dark matter inner slope than the case of HST 14113+5211.

We also obtain the most likely fraction of the dark matter projected inside R_E ($\simeq 2.9R_e$) for the isotropic velocity case, yielding $f_{DM} = 0.89^{+0.06}_{-0.04}$ (without the FP constraints) and $0.86^{+0.05}_{-0.03}$ (with the FP constraints). Thus, in contrast to the case of HST 14113+5211, the total mass inside R_E derived from the lens model is totally dominated by dark matter; some of this unseen mass component may be provided

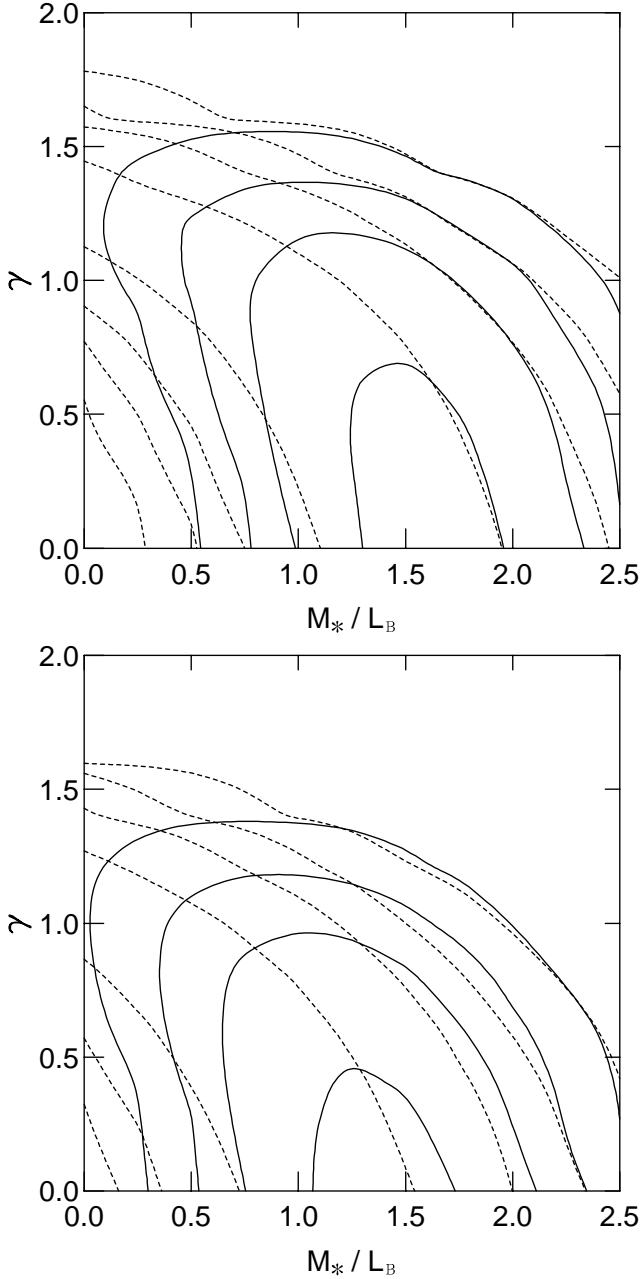


Figure 7. The same as Fig.5 but for B 2045+265.

by the group of galaxies which the lensing galaxy belongs to.

For a single-component mass model (Figure 8), we obtain the most likely values of γ' for $r_i = R_e$ (Model A) and $\beta = 0$ (Model B), yielding $1.58^{+0.08}_{-0.09}$ and $1.66^{+0.07}_{-0.08}$, respectively. Thus, the model prediction for the slope of the total density profile is systematically flatter than isothermal.

6 DISCUSSION AND CONCLUDING REMARKS

As explored in this work and also in TK04, the mass-to-light ratio for both of our targets based on the joint lensing and dynamical analysis is virtually consistent with that ob-

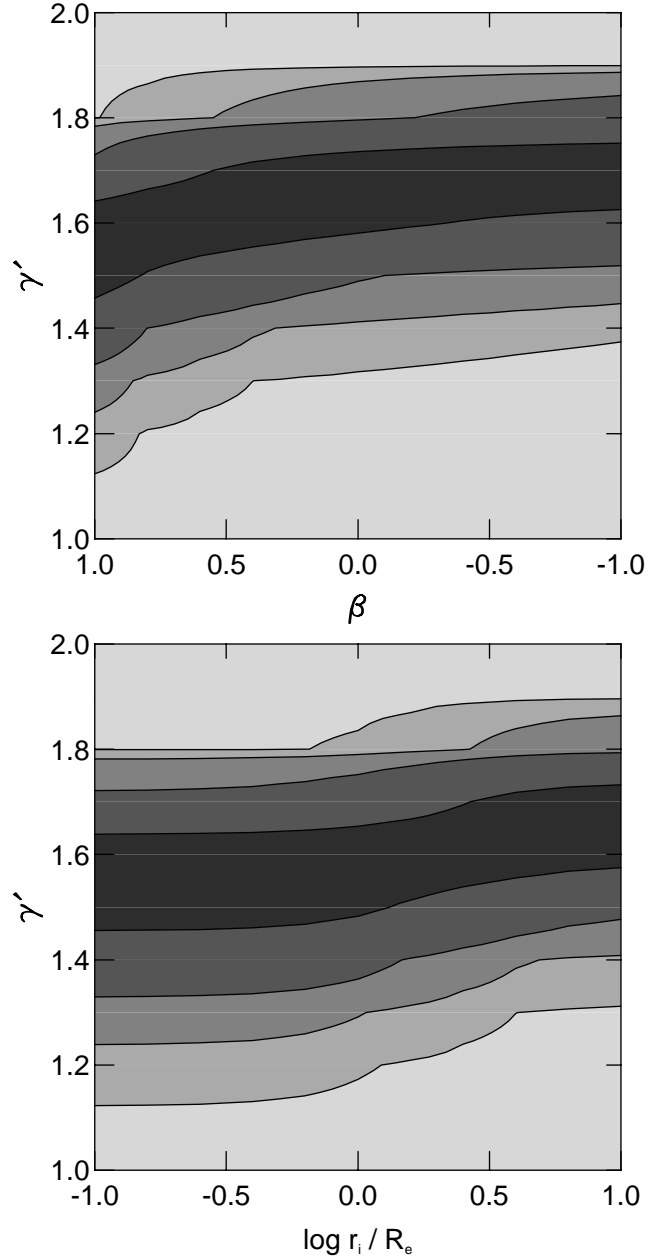


Figure 8. The same as Fig.6 but for B 2045+265.

tained from the FP constraint; the mass-to-light ratios at $z_L = 0.464$ and 0.868 are systematically smaller than the current average value of $(M_*/L_B)_0 = 7.3 \pm 2.1 h_{65} M_{\odot}/L_{B,\odot}$ (Gerhard et al. 2001), implying the aging of stellar populations from these redshifts to the present day. For comparison with other sample lenses for which the similar analysis has been employed, we plot, in Figure 9, the redshift evolution of the stellar mass-to-light ratio for both of our targets (open circles) and the TK04 sample (solid circles). It is found that the current sample lenses follow the general redshift evolution of M_*/L_B , as guided by the solid and dashed lines showing the average evolution of M_*/L_B derived from the FP of early-type lensing galaxies by TK04 and Rusin et al. (2003), respectively.

The inner slope of the dark-matter halos, γ , ranges from

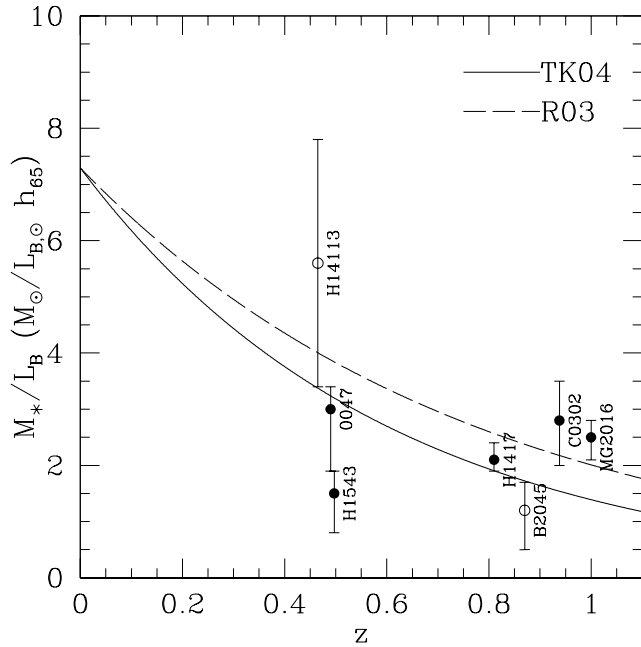


Figure 9. Redshift evolution of the stellar mass-to-light ratio. The open circles correspond to HST 14113+5211 and B 2045+265 derived from the current lensing model (for an isotropic velocity) without the FP constraints, whereas the solid circles are taken from TK04 with the same models. The solid and dashed lines show the average evolution of M_*/L_B derived from the FP of early-type lensing galaxies by TK04 and Rusin et al. (2003), respectively.

0.0 to 1.8. More specifically, the most likely values of γ (with the FP constraints) for HST 14113+5211 are $0 < \gamma < 1.6$ ($0 < \gamma < 1.8$) at 1σ for Model A (Model B), whereas for B 2045+265, we obtain $0 < \gamma < 0.5$ ($0 < \gamma < 0.8$) at 1σ for Model A (Model B). These values are consistent with the density slopes of dark halos predicted by cosmological N-body simulations, showing γ of 1.0 to 1.5 (e.g., Navarro, Frenk, and White 1995; Moore et al. 1998; Fukushige & Makino 2003 and references therein), although the present-day inner slope of the dark-matter halos is affected by the effect of baryonic infall to some extent; the effect seems to be not so significant as obtained from other lens samples (TK04). It is also drawn that the inner slope of the dark-matter halos is systematically flatter than an isothermal profile.

The index for a single power-law model (γ') is almost 2 for HST 14113+5211, thereby suggesting that a singular isothermal model is a good fit to this lensing galaxy. For B 2045+265, γ' ranges from 1.5 to 1.7, which is systematically flatter than isothermal (Figure 8). This flat slope is related to the very small velocity dispersion of stars $\sigma = 213 \text{ km s}^{-1}$ compared with $\sigma_{\text{SIE}} = 397 \text{ km s}^{-1}$; a flatter slope of a dark halo than SIE is needed to reduce the radial gravitational force and thus the velocity dispersion of stars. Alternatively, some part of $M(< R_E)$ for B 2045+265 is provided by the group of galaxies, thereby causing a large value of σ_{SIE} . This effect may partly contribute to a non-negligible scatter of γ' from an isothermal index (2) as is also reported in other lens samples (TK04).

ACKNOWLEDGMENTS

This work has been supported in part by a Grant-in-Aid for Scientific Research (15540241, 16740118 and 177401166827) of the Ministry of Education, Culture, Sports, Science and Technology in Japan.

REFERENCES

- Bender, R. et al. 1998, *ApJ*, 493, 529
 Binney, J. Tremaine, S. 1987, *Galactic Dynamics*, Princeton University Press, Princeton
 Coleman, G. D., Wu, C.-C., Weedman, D. W. 1980, *ApJS*, 43, 393
 Falco, E. E., Shapiro, I. I., Moustakas, L. A., Davis, M. 1997, *ApJ*, 484, 70
 Fassnacht, C. D. et al. 1999, *AJ*, 117, 658
 Fischer, P., Schade, D., Barrientos, L. F. 1998, *ApJ*, 503, L127 (F98)
 Fukushige T., Makino J., 2003, *ApJ*, 588, 674
 Gerhard, O., Kronawitter, A., Saglia, R. P., Bender, R. 2001, *AJ*, 121, 1936
 Hernquist, L. 1990, *ApJ*, 356, 359
 Iye, M., et al. 2004, *PASJ*, 54, 833
 Kashikawa N., et al. 2002, *PASJ*, 54, 819
 Keeton, C. R., Kochanek, C. S., Seljak, U., 1997, *ApJ*, 482, 604
 Keeton, C. R., Kochanek, C. S., Falco, E. E., 1998, *ApJ*, 509, 561
 Kochanek, C. S., 1991, *ApJ*, 373, 354
 Kochanek, C. S. et al. 2000, *ApJ*, 543, 131
 Koopmans L. V. E., Treu T., 2003, *ApJ*, 583, 606
 Kormann, R., Schneider, P., Bartelmann, M. 1994, *A&A*, 284, 285
 Leitherer C. et al., 1996, *PASP*, 108, 996
 Lubin, L. M. et al. 2000, *AJ*, 119, 451
 Moore B., Governato F., Quinn T., Statal J., Lake G., 1998, *ApJ*, 499, L5
 Navarro, J. F., Frenk, C. S., White, S. D. M. 1995, *MNRAS*, 275, 56 (NFW)
 Ohyama, Y. et al. 2002, *AJ*, 123, 2903
 Rusin, D. et al. 2003, *ApJ*, 587, 143
 Schlegel D. J., Finkbeiner D. P., Davis M., 1998, *ApJ*, 500, 525
 Schmidt, M., Schneider, D. P., Gunn, J. E. 1995, *AJ*, 110, 68
 Schneider, P., Ehlers, J., Falco, E. E. 1992, *Gravitational Lenses* (Berlin: Springer)
 Spergel, D. N. et al. 2003, *ApJS*, 148, 175
 Tonry, J. L. 1998, *ApJ*, 115, 1
 Tonry, J. L., Davis, M. 1979, *AJ*, 84, 1511
 Treu, T., Koopmans, L. V. E. 2002, *ApJ*, 575, 87
 Treu, T., Koopmans, L. V. E. 2004, *ApJ*, 611, 739 (TK04)
 van de Ven, G., van Dokkum, P. G., Franx, M. 2003, *MNRAS*, 344, 924 (vdV03)
 van Dokkum, P. G., Franx, M., Kelson, D. D., Illingworth, G. D. 1998, *ApJ*, 504, L7
 van Dokkum, P. G., Franx, M. 1996, *MNRAS*, 281, 985
 Yoshida, M., et al. 2000, *SPIE*, 4009, 240

APPENDIX A: ESTIMATION OF THE LENS LUMINOSITY IN THE B BAND

For the lensing galaxy of HST 14113+5211, F98 reported the F702W(AB) magnitude as 20.78 ± 0.05 mag. Based on the K-correction using Coleman, Wu, & Weedman (1980) and the assumption of no galaxy evolution, F98 derived the absolute B magnitude as $M_B(AB) = -19.32 + 5 \log h$ for $(\Omega_0, \lambda_0) = (1, 0)$ and $z_L = 0.46$. Then, we transform this magnitude into Vega-based B magnitude [$M_B(\text{Vega}) = M_B(AB) + 0.12$, Schmidt, Schneider, & Gunn 1995] and consider the revised lens redshift of $z_L = 0.464$ (Lubin et al. 2000) and cosmological parameters of $(\Omega_0, \lambda_0) = (0.3, 0.7)$ (Spergel et al. 2003). We thus obtain $M_B = -19.60 + 5 \log h$, giving the luminosity of $L_B/L_{B,\odot} = 2.6 \times 10^{10}$ ($h = 0.65$) for the lensing galaxy of HST 14113+5211.

For the lensing galaxy of B 2045+265, Fassnacht et al. (1999) reported the various infrared magnitudes in a $1.''9$ diameter aperture (corresponding to the size of the Einstein ring in their lens model). Based on the K-correction for an Sa galaxy as the lens appears to show its typical spectrum, they arrived at the rest-frame *B*-band luminosity of $2.36 \times 10^{10} h^{-2} L_\odot$ in this aperture for $(\Omega_0, \lambda_0) = (1, 0)$. To derive the total *B*-band luminosity, we adopt the work of Rusin et al. (2003), where they obtained the intermediate-axis effective radius (R_e) determined by fitting the observed brightness distribution to a de Vaucouleurs profile. Using their R_e of $0.''38$ and $(\Omega_0, \lambda_0) = (0.3, 0.7)$, we obtain the luminosity of $L_B/L_{B,\odot} = 1.3 \times 10^{11}$ ($h = 0.65$) for the lensing galaxy of B 2045+265.